Three-dimensional ground based imaging radar based on C-band cross-MIMO array and tensor compressive sensing

Weike Feng, *Student member, IEEE*, Jean-Michel Friedt, Giovanni Nico, *Senior Member, IEEE*, and Motoyuki Sato, *Fellow, IEEE*

***Abstract*—We designed a ground based radar system with a C-band two-dimensional cross multiple input multiple output (MIMO) array for three-dimensional imaging and displacement estimation purpose. For this system, we developed a far-field pseudo-polar image format algorithm using pseudo-polar spherical coordinate. The use of a tensor compressive sensing technique allows to focus under-sampled raw data and to optimize the data acquisition time and memory usage. A novel algorithm, named as tensor based iterative adaptive approach, is proposed for the effective and efficient reconstruction of sparse targets with a reduced level of sidelobes. Experiment results validate the designed radar system and the proposed algorithms.**

***Index Terms*—Three-dimensional (3D) imaging, cross multiple input multiple output (MIMO), compressive sensing, pseudo-polar spherical coordinate, iterative adaptive approach.**

I. Introduction

Ground based synthetic aperture radar (GBSAR) is a powerful technique to monitor displacement, deformation, and vibration of terrain and infrastructure with an accuracy of sub-millimeter [1-2]. In GBSAR, a one-dimensional (1D) synthetic aperture is normally formed by sequentially moving the transceiver on a rail to get a high angle resolution. In recent years, linear multiple input multiple output (MIMO) array based methods have been proposed [3-4], which can reduce the data acquisition period of GBSAR, benefiting some specific applications where it is necessary to do many measurements within a short time. Besides, a shorter data acquisition time is also useful to mitigate the phase artifacts caused by microwave propagation in atmosphere on the displacement estimation.

Characterized by a highly suboptimal aperture compared with the airborne/spaceborne SAR, several imaging algorithms were developed to focus GBSAR data, including time-domain back projection algorithm (TDBP), frequency-domain back projection algorithm, range migration algorithm, and far-field pseudo-polar format algorithm (FPFA) [5]. For MIMO array based radar, these algorithms can be adopted with simple modifications [6-7]. Compared with other imaging algorithms, despite being only applicable in the far field, FPFA has the great advantage of computation complexity, especially when the aperture length is comparable to the range resolution [8-9].

Since only 1D aperture is synthesized, GBSAR can only get a two-dimensional (2D) focused SAR image. In such a case, the 3D scene is projected onto a 2D imaging plane, resulting in some information losses. Normally, for the applications of GBSAR to dam and landslide monitoring, an accurate digital elevation model (DEM) is needed for the accurate positioning of targets that have large displacements [1]. However, the unambiguity requirement always makes the projection of the 2D GBSAR image onto the DEM a complicated task. Moreover, an accurate DEM is not always available. Therefore, a GBSAR system that can get the 3D focused image is desired, which requires a 2D synthetic aperture. Two simple ways are possible to get a 2D aperture: 1) mechanically move the transceiver on a 2D scanner, and 2) similarly with the MIMO-SAR system [10-11], using a linear MIMO array moved on a mechanical rail. However, the data sampling time of these two approaches is normally too long for many applications.

In this paper, we present a 3D volumetric imaging GBSAR system with a 2D cross-MIMO array. Compared with other 2D MIMO configurations, cross-MIMO is easier to implement in practice. According to the signal model in far-range condition, we established a pseudo-polar spherical coordinate, based on which the FPFA algorithm is extended to its 3D version for effective 3D imaging. When the imaging scene is sparse, i.e. only several targets have significant reflection coefficients, we proposed a tensor compressive sensing (T-CS) [12-13] based imaging algorithm to shorten data acquisition time, reduce memory usage, and improve imaging quality. Furthermore, a tensor based iterative adaptive approach [14-16] (T-IAA) is proposed to solve the T-CS problem efficiently and accurately. Experiment results are presented to show the effectiveness of the designed radar system and the proposed algorithms.

This work was supported by JSPS Grant-in-Aid for Scientific Research (A) 26249058.

Weike Feng is with the Graduate School of Environmental Studies, Tohoku University, 980-8579, Sendai, Japan (e-mail: feng.weike.q4@dc.tohoku.ac.jp).

Jean-Michel Friedt is with the FEMTO-ST, Time & Frequency department, Besancon, France (e-mail: jean-michel.friedt@femto-st.fr).

Giovanni Nico is with Istituto per le Applicazioni del Calcolo (IAC), Consiglio Nazionale delle Ricerche (CNR), Bari, Italy (e-mail: g.nico@ba.iac.cnr.it).

Motoyuki Sato is with the Center for Northeast Asian Studies, Tohoku University, 980-8576, Sendai, Japan (e-mail: motoyuki.sato.b3@tohoku.ac.jp).

II. Radar System and Signal Model

The configuration of the designed radar system is shown in Fig. 1, which mainly includes a vector network analyzer (VNA) to generate the frequency stepped continuous wave (FSCW) signal, four 1×8 switches to realize the time-divided signal transmitting and receiving, two micro-controllers used to control the switches, a uniform receiving array with 16 Vivaldi antennas, a uniform transmitting array with 16 spiral antennas, and a processing PC used to save and process the VNA data and to remotely control the micro-controllers and the VNA.

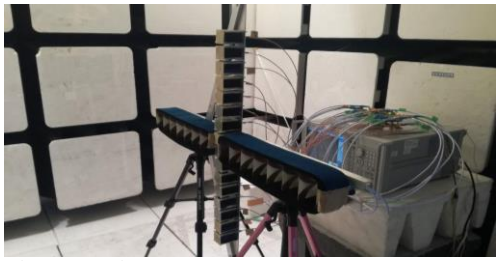

Fig. 1. Configuration of the 3D imaging radar system.

The imaging geometry of the designed system is shown in Fig. 2, where the i-th receiver is at $(x_i, 0, 0)$, the j-th transmitter is at $(0, 0, z_j)$, i=1,2,…,16, and j=1,2,…,16. With a target located at (x_0, y_0, z_0), the distance between the i-j-th sampling point and the target is given by

$$R_{i,j}^0=\sqrt{(x_i-x_0)^2+y_0^2+z_0^2}+\sqrt{x_0^2+y_0^2+(z_j-z_0)^2} \tag{1}$$

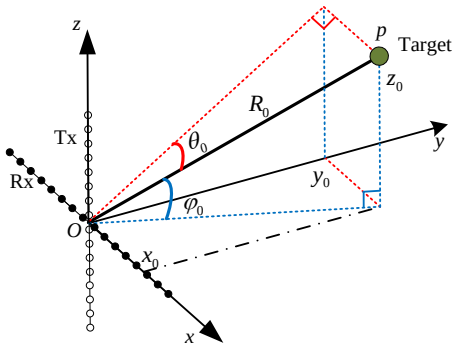

Fig. 2. Imaging geometry of the designed radar system.

Then, with the FSCW transmitted signal, the received signal at i-j-th sampling point and q-th frequency can be expressed as

$$s_0(i,j,q)=\alpha_0\exp(-\mathrm{j}2\pi f_q R_{i,j}^0/c)+n_0(i,j,q) \tag{2}$$

where f_q=f_0+(q-1)Δf, q=1,2,...,Q, f_0 is the start frequency, Δf is the frequency step, α_0 is the reflection coefficient of the target, c is the velocity of light, and $n_0(i,j,q)$ is the additive noise.

Therefore, the received signal from the whole illuminated scene is given by

$$s(i,j,q)=\iiint_{\Omega}\alpha(x,y,z)e^{-\mathrm{j}2\pi f_q R_{i,j}(x,y,z)/c}\mathrm{d}x\mathrm{d}y\mathrm{d}z+n(i,j,q) \tag{3}$$

where $R_{i,j}(x,y,z)$ is the distance between the target at (x, y, z) and i-jth sampling point, $\alpha(x,y,z)$ is the reflection coefficient, and Ω denotes the illuminated scene.

According to [4], the reflection coefficient of target at (x, y, z) can be estimated by the BP algorithm as follows:

$$\alpha(x,y,z)=\sum_{i=1}^{I}\sum_{j=1}^{J}\sum_{q=1}^{Q}s(i,j,q)e^{+\mathrm{j}2\pi f_q R_{i,j}(x,y,z)/c} \tag{4}$$

However, the estimation of the entire illuminated scene using (4) has a high computation complexity, which prevents it from practical applications. Therefore, a faster algorithm is needed.

III. Fast 3D Imaging Algorithm

A. 3D Pseudopolar coordinate

In Fig. 2, let $R_0=\sqrt{x_0^2+y_0^2+z_0^2}$ denote the distance from the center of radar system to the target, θ_0 denote the angle between op and the y-o-z plane (*i.e.* azimuth angle), and φ_0 denote the angle between op and the x-o-y plane (*i.e.* elevation angle), we have $x_0=R_0\sin\theta_0$ and $z_0=R_0\sin\varphi_0$. Based on the cosine theorem, the distance between i-j-th sampling point and the target located at far field can be approximated as

$$R_{i,j}^0\simeq 2R_0-\sin\theta_0 x_i-\sin\varphi_0 z_j \tag{5}$$

Therefore, the reflection coefficient of the target at (R, θ, φ) can be estimated by

$$\alpha(R,\theta,\varphi)\simeq\sum_{i=1}^{I}\sum_{j=1}^{J}\sum_{q=1}^{Q}s(i,j,q)e^{\mathrm{j}2\pi f_q\frac{2R}{c}}e^{-\mathrm{j}2\pi x_i\frac{\sin\theta}{\lambda_c}}e^{-\mathrm{j}2\pi z_j\frac{\sin\varphi}{\lambda_c}}e^{-\mathrm{j}\psi_{i,j,q}} \tag{6}$$

where $\psi_{i,j,q}=2\pi f_q(\sin\theta x_i+\sin\varphi z_j)/c$, $f_q=f_q-f_c$, f_c is the center frequency, and $\lambda_c=c/f_c$ is the wavelength.

The absolute value of $\psi_{i,j,q}$ in (6) is bounded by

$$\left|\psi_{i,j,q}\right|=\left|2\pi f_q(\sin\theta x_i+\sin\varphi z_j)/c\right|\le\frac{\pi(\sin\theta L_x+\sin\varphi L_z)}{4\Delta R} \tag{7}$$

where $\Delta R=c/2B$ is the range resolution, B is the bandwidth, L_x and L_z are the synthetic aperture length in x direction and z direction, respectively. As analyzed in [9], if $\left|\psi_{i,j,q}\right|$ satisfies the condition (8), the last exponential term of (6) can be ignored.

$$\left|\psi_{i,j,q}\right|\le\frac{\pi}{2}\Rightarrow\frac{(L_x\sin\theta_{\max}+L_z\sin\varphi_{\max})}{2\Delta R}\le 1 \tag{8}$$

For the designed radar system, $(L_x\sin\theta_{\max}+L_z\sin\varphi_{\max})$ is close to $2\Delta R$. Besides, since the mean value of x_i (z_j) is zero and due to the factors sinθ and sinφ, $\psi_{i,j,q}$ is smaller than those given in (8) [8]. Therefore, the reflection coefficient of the target at (R, θ, φ) can be approximately estimated by

$$\alpha(R,\theta,\varphi)\simeq\sum_{i=1}^{I}\sum_{j=1}^{J}\sum_{q=1}^{Q}s(i,j,q)e^{\mathrm{j}2\pi f_q\frac{2R}{c}}e^{-\mathrm{j}2\pi x_i\frac{\sin\theta}{\lambda_c}}e^{-\mathrm{j}2\pi z_j\frac{\sin\varphi}{\lambda_c}} \tag{9}$$

It can be observed that the exponential terms in (9) form the kernel of a 3D Fourier transform. Therefore, a 3D pseudopolar spherical coordinate (α,β,γ) is defined as

$$\alpha=2R/c,\quad \beta=\sin\theta/\lambda_c,\quad \gamma=\sin\varphi/\lambda_c \tag{10}$$

Based on this pseudopolar coordinate, the received signal cube and the 3D FPFA algorithm can be formulated as the following multilinear expression:

$$\underline{\boldsymbol{S}}=\underline{\boldsymbol{A}}\times_1\boldsymbol{F}_1\times_2\boldsymbol{F}_2\times_3\boldsymbol{F}_3 \tag{11}$$

and

$$\underline{\boldsymbol{A}}=\underline{\boldsymbol{S}}\times_1\boldsymbol{F}_1^{\mathrm{H}}\times_2\boldsymbol{F}_2^{\mathrm{H}}\times_3\boldsymbol{F}_3^{\mathrm{H}}=FFT_{3\mathrm{D}}\left[\underline{\boldsymbol{S}}\right] \tag{12}$$

where $(\cdot)^{\mathrm{H}}$ denotes conjugate transpose, $\times_\kappa$ denotes the mode-κ tensor by matrix product [17], $\underline{\boldsymbol{S}}$ is the received signal cube, $\underline{\boldsymbol{A}}$ is the reflection coefficient tensor of the imaging scene, $\boldsymbol{F}_1$,

$\boldsymbol{F}_2$, and $\boldsymbol{F}_3$ are the Fourier transform matrices.

Compared to (4) and (6), the proposed 3D FPFA focusing algorithm (12) can significantly reduce the computational cost by using the fast Fourier transform (FFT). However, due to the intrinsic limitation of Fourier transform based methods, high-level sidelobes will be generated by (12), which will blur the weak targets and thus introduce negative influence on the following displacement estimation.

B. Tensor based IAA

When the imaging scene is sparse, i.e. only few strong targets exist, T-CS based method can be used for 3D imaging as shown in (13), which can reduce the sidelobe level and achieve higher resolution than Fourier transform based imaging methods [12].

$$\underline{\boldsymbol{A}}=\min\|\underline{\boldsymbol{A}}\|_0 \quad \text{s.t. } \|\underline{\boldsymbol{S}}-\underline{\boldsymbol{A}}\times_1\boldsymbol{F}_1\times_2\boldsymbol{F}_2\times_3\boldsymbol{F}_3\|_{\underline{F}}\le\varepsilon \tag{13}$$

where ε denotes the noise level, $\|\cdot\|_0$ denotes the number of nonzero elements in a vector or a tensor, and the Frobenius norm of a tensor $\underline{\boldsymbol{Y}}$ is defined as $\|\underline{\boldsymbol{Y}}\|_{\underline{F}}\triangleq\sqrt{\sum_{i_1}\sum_{i_2}\sum_{i_3}|y_{i_1,i_2,i_3}|^2}$.

One advantage of T-CS based imaging method is that it can still work well with under-sampled data, which can help to reduce the data acquisition time, the computation complexity, and the memory usage of (13). For the designed radar system, to reduce the spatial sampling points in x and z directions, a data acquisition program is used to control the switches to randomly turn on several transmitter-receiver pairs of the cross MIMO array. Since the frequencies of the FSCW signal cannot be randomly generated by VNA, the frequency under-sampling is realized in the data processing step. The random selection of frequencies by using a discrete frequency synthesizer driven by a set of random indication numbers is under study.

The under-sampled signal model, i.e. the compressive measurement of target reflection coefficient tensor, is shown in Fig. 3, where $\underline{\boldsymbol{S}}^{un}$ is the under-sampled received signal cube, $\boldsymbol{F}_1^{un}$, $\boldsymbol{F}_2^{un}$ and $\boldsymbol{F}_3^{un}$ are the under-sampled Fourier transform matrices.

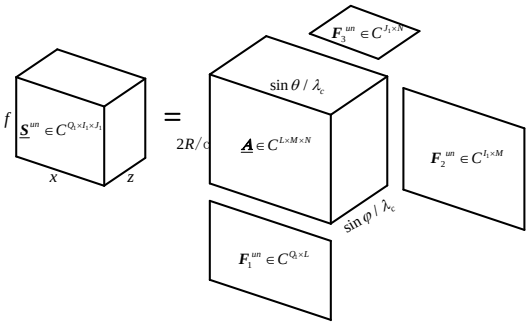

Fig. 3. Compressive measurement of the target reflection coefficient tensor.

Then, the focused image of targets can be obtained by

$$\underline{\boldsymbol{A}}=\min\|\underline{\boldsymbol{A}}\|_0 \quad \text{s.t. } \|\underline{\boldsymbol{S}}^{un}-\underline{\boldsymbol{A}}\times_1\boldsymbol{F}_1^{un}\times_2\boldsymbol{F}_2^{un}\times_3\boldsymbol{F}_3^{un}\|_{\underline{F}}\le\varepsilon \tag{14}$$

Eq. (14) is NP-hard but can be solved by some efficient algorithms, such as the Kronecker-orthogonal matching pursuit (Kron-OMP) algorithm and the N-way Block OMP algorithm (NBOMP) in [13], and the 3D smoothed l_0 norm algorithm (3D-SL0) in [12]. However, Kron-OMP and NBOMP need to know the number of targets or the noise power, which is commonly unknown in practice. For 3D-SL0 algorithm, several parameters need to be tuned, which requires a lot of efforts in some cases. Therefore, based on the principle of IAA algorithm [14] and its efficient 2D version [15], we propose a nonparametric and user parameter-free algorithm, called T-IAA algorithm, to solve (14).

Conventionally, to fit the classical CS theory, $\underline{\boldsymbol{A}}$ is vectorized and estimated by the following 1D minimization problem.

$$\boldsymbol{\alpha}=\min\|\boldsymbol{\alpha}\|_0 \quad \text{s.t. } \|\boldsymbol{s}^{un}-\boldsymbol{\Psi}\boldsymbol{\alpha}\|_2\le\varepsilon \tag{15}$$

where $\boldsymbol{\Psi}=\boldsymbol{F}_3^{un}\otimes\boldsymbol{F}_2^{un}\otimes\boldsymbol{F}_1^{un}$, $\boldsymbol{s}^{un}=vec(\underline{\boldsymbol{S}}^{un})$, $\boldsymbol{\alpha}=vec(\underline{\boldsymbol{A}})$, $\otimes$ denotes Kronecker product, and $vec(\cdot)$ denotes the vectorization operation. IAA attempts to solve (15) by minimizing the following weighted least-squares cost function.

$$\boldsymbol{\alpha}_b=\min\|\boldsymbol{s}^{un}-\boldsymbol{\alpha}_b\boldsymbol{\psi}_b\|_{\boldsymbol{Q}_b^{-1}}^2 \tag{16}$$

where $\boldsymbol{\alpha}_b$ is the b-th element of $\boldsymbol{\alpha}$, $\boldsymbol{\psi}_b$ is the b-th column of $\boldsymbol{\Psi}$, $\|\boldsymbol{x}\|_{\boldsymbol{Q}_b^{-1}}^2\triangleq\boldsymbol{x}^{\mathrm{H}}\boldsymbol{Q}_b^{-1}\boldsymbol{x}$, $\boldsymbol{Q}_b=\boldsymbol{R}-|\boldsymbol{\alpha}_b|^2\boldsymbol{\psi}_b\boldsymbol{\psi}_b^{\mathrm{H}}$, and $\boldsymbol{R}$ is the covariance matrix of $\boldsymbol{s}^{un}$. The minimization of (16) yields

$$\boldsymbol{\alpha}_b=\boldsymbol{\psi}_b^{\mathrm{H}}\boldsymbol{R}^{-1}\boldsymbol{s}^{un}/\boldsymbol{\psi}_b^{\mathrm{H}}\boldsymbol{R}^{-1}\boldsymbol{\psi}_b \tag{17}$$

Due to the unknown $\boldsymbol{R}$, IAA algorithm operates iteratively to get (17). For most practical applications, convergence occurs after no more than 10-15 iterations [15]. The initialization of IAA algorithm is $\boldsymbol{\alpha}_b^0=\boldsymbol{\psi}_b^{\mathrm{H}}\boldsymbol{s}^{un}/\boldsymbol{\psi}_b^{\mathrm{H}}\boldsymbol{\psi}_b$, and the o-th (o=1,2,…,O) iteration is carried out by

$$\boldsymbol{\alpha}_b^o=\boldsymbol{\psi}_b^{\mathrm{H}}(\boldsymbol{\Psi}\boldsymbol{\Pi}^{o-1}\boldsymbol{\Psi}^{\mathrm{H}})^{-1}\boldsymbol{s}^{un}/\boldsymbol{\psi}_b^{\mathrm{H}}(\boldsymbol{\Psi}\boldsymbol{\Pi}^{o-1}\boldsymbol{\Psi}^{\mathrm{H}})^{-1}\boldsymbol{\psi}_b \tag{18}$$

where $\boldsymbol{\Pi}^{o-1}=diag\{|\boldsymbol{\alpha}^{o-1}|^2\}$ and $(\cdot)^{-1}$ denotes matrix inverse.

Based on the Capon filter property, the vector form of (18) is given by [14]

$$\boldsymbol{\alpha}^o\simeq\boldsymbol{\Pi}^{o-1}\boldsymbol{\Psi}^{\mathrm{H}}(\boldsymbol{\Psi}\boldsymbol{\Pi}^{o-1}\boldsymbol{\Psi}^{\mathrm{H}})^{-1}\boldsymbol{s}^{un}=\boldsymbol{\Pi}^{o-1}\boldsymbol{\Psi}^{\mathrm{H}}\boldsymbol{u}^{o-1} \tag{19}$$

where $\boldsymbol{u}^{o-1}\simeq(\boldsymbol{\Psi}\boldsymbol{\Pi}^{o-1}\boldsymbol{\Psi}^{\mathrm{H}})^{-1}\boldsymbol{s}^{un}$ is obtained by conjugate gradient (CG) algorithm to reduce the computation cost.

Assuming $\underline{\boldsymbol{\Sigma}}^{o-1}=|\underline{\boldsymbol{\Lambda}}^{o-1}|^2$, it can be derived that

$$\boldsymbol{\Pi}^{o-1}=diag\{vec(\underline{\boldsymbol{\Sigma}}^{o-1})\} \tag{20}$$

where $diag(\cdot)$ denotes diagonalization.

Therefore, based on $\boldsymbol{\Psi}=\boldsymbol{F}_3^{un}\otimes\boldsymbol{F}_2^{un}\otimes\boldsymbol{F}_1^{un}$ and the properties of Kronecker product and Hadamard product, we can obtain

$$\boldsymbol{\alpha}^o\simeq vec(\underline{\boldsymbol{\Sigma}}^{o-1}\odot[\underline{\boldsymbol{U}}^{o-1}\times_1(\boldsymbol{F}_1^{un})^{\mathrm{H}}\times_2(\boldsymbol{F}_2^{un})^{\mathrm{H}}\times_3(\boldsymbol{F}_3^{un})^{\mathrm{H}}]) \tag{21}$$

where $\underline{\boldsymbol{U}}^{o-1}$ is the tensor form of $\boldsymbol{u}^{o-1}$ that can be obtained by the tensor version of CG algorithm, as shown in Table. 1, $(\cdot)^*$ denotes conjugate, and $\odot$ denotes Hadamard product.

TABLE I. TENSOR BASED CG ALGORITHM.

Input: $\underline{\boldsymbol{S}}^{un}$, $\boldsymbol{F}_1^{un}$, $\boldsymbol{F}_2^{un}$, $\boldsymbol{F}_3^{un}$, $\underline{\boldsymbol{\Sigma}}^{o-1}$, and the iterations number T.

1) Initialization: $\underline{\boldsymbol{U}}^0=0,\beta_0=0,\underline{\boldsymbol{R}}_0=\underline{\boldsymbol{S}}^{un},P_0=0,\rho_0=|\underline{\boldsymbol{R}}_0|_{\underline{F}}^2$, and $t=1$;

2) Update:

$$\underline{\boldsymbol{P}}_t=\underline{\boldsymbol{R}}_{t-1}+\beta_{t-1}\underline{\boldsymbol{P}}_{t-1},\ \underline{\boldsymbol{T}}_1=\underline{\boldsymbol{\Sigma}}^{o-1}\odot[\underline{\boldsymbol{P}}_t\times_1(\boldsymbol{F}_1^{un})^{\mathrm{H}}\times_2(\boldsymbol{F}_2^{un})^{\mathrm{H}}\times_3(\boldsymbol{F}_3^{un})^{\mathrm{H}}],$$

$$\underline{\boldsymbol{T}}_2=\underline{\boldsymbol{T}}_1\times_1\boldsymbol{F}^{un}{}_1\times_2\boldsymbol{F}_2^{un}\times_3\boldsymbol{F}_3^{un},\ \alpha_{t-1}=\rho_{t-1}/\sum\sum\sum\underline{\boldsymbol{P}}_t^*\odot\underline{\boldsymbol{T}}_2,$$

$$\underline{\boldsymbol{U}}_t=\underline{\boldsymbol{U}}_{t-1}+\alpha_{t-1}\underline{\boldsymbol{P}}_t,\ \underline{\boldsymbol{R}}_t=\underline{\boldsymbol{R}}_{t-1}-\alpha_{t-1}\underline{\boldsymbol{T}}_2,\ \rho_t=|\underline{\boldsymbol{R}}_t|_{\underline{F}}^2,\ \beta_t=\rho_t/\rho_{t-1}.$$

3) Iteration: $t\leftarrow t+1$, if $t\le T$ go back to 2), otherwise, stop.

Output: $\underline{\boldsymbol{U}}^{o-1}=\underline{\boldsymbol{U}}^T$.

Since $\boldsymbol{\alpha}^o=vec(\underline{\boldsymbol{\Lambda}}^o)$, the tensor based IAA algorithm can be derived as shown in Table. 2, in which the initialization step is

obtained by making use of the minimum l_2-norm solution and $(\cdot)^{\dagger}$ denotes pseudo-inversion.

TABLE II. TENSOR BASED IAA ALGORITHM.

Input: $\underline{\boldsymbol{S}}^{un}$, $\boldsymbol{F}_1^{un}$, $\boldsymbol{F}_2^{un}$, $\boldsymbol{F}_3^{un}$, and the iterations number O and T.
1) Initialization: $\underline{\boldsymbol{\Lambda}}^{0} = \underline{\boldsymbol{S}}^{un} \times_1 (\boldsymbol{F}_1^{un})^{\dagger} \times_2 (\boldsymbol{F}_2^{un})^{\dagger} \times_3 (\boldsymbol{F}_3^{un})^{\dagger}$, $\underline{\boldsymbol{\Sigma}}^{0} = \lvert \underline{\boldsymbol{\Lambda}}^{0} \rvert^2$, and $o = 1$;
2) Estimation: with $\underline{\boldsymbol{S}}^{un}$, $\boldsymbol{F}_1^{un}$, $\boldsymbol{F}_2^{un}$, $\boldsymbol{F}_3^{un}$ and $\underline{\boldsymbol{\Sigma}}^{o-1}$ as inputs, use Tensor based CG to estimate $\underline{\boldsymbol{U}}^{o-1}$ within T iterations;
3) Update: $\underline{\boldsymbol{\Lambda}}^{o} = \underline{\boldsymbol{\Sigma}}^{o-1} \odot [\underline{\boldsymbol{U}}^{o-1} \times_1 (\boldsymbol{F}_1^{un})^{\mathrm{H}} \times_2 (\boldsymbol{F}_2^{un})^{\mathrm{H}} \times_3 (\boldsymbol{F}_3^{un})^{\mathrm{H}}]$ and $\underline{\boldsymbol{\Sigma}}^{o} = \lvert \underline{\boldsymbol{\Lambda}}^{o} \rvert^2$;
4) Iteration: $o \leftarrow o+1$, if $o \le O$ go back to 2), otherwise, stop.
Output: $\underline{\boldsymbol{\Lambda}} = \underline{\boldsymbol{\Lambda}}^{O}$.

IV. EXPERIMENT RESULTS

In this section, we present some experiment results to illustrate the effectiveness of the designed system and the proposed imaging algorithms. It should be pointed out that, to improve the imaging quality, the antenna direct coupling signal of the designed system is measured in an anechoic chamber and then subtracted from the real measurement data. The working frequency of the designed system is from 4.75 to 5.25 GHz with 201 frequency steps, giving a range resolution of 0.3 m. Due to the antenna size limitation, the inter-element spacing of the transmitting array and the receiving array are set to be 5 cm and 6 cm, respectively, giving an unambiguous angle about 60 degrees. The resolution in x direction is about 0.067 rad, and the resolution in z direction is about 0.080 rad. The point spread function of the designed cross-MIMO radar system for a target located at (10, 0, 0) can be obtained as shown in Fig. 4.

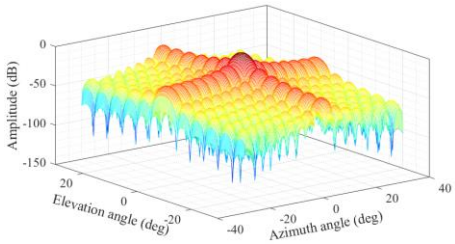

Fig. 4. Point spread function of the designed system for a target at (10, 0, 0).

Fig. 5. Experiment with two trihedral corner reflectors as targets.

Firstly, two trihedral corner reflectors (CRs) with size 40 cm and 30 cm are used as the point targets. They are located at (0, 6.5, 0) m and (1, 9.5, 0.5) m approximately. The experiment setup is shown in Fig. 5 and the focused images obtained by BP algorithm, 3D FPFA algorithm, 3D FPFA algorithm together with spatially variant apodization (SVA) [18] approach, and T-IAA algorithm (for which we set O=T=10) with 1/8 data are shown in Fig. 6, where the coordinate is same as Fig. 2 and the dynamic range is 20 dB.

It can be seen from Fig. 6 (a) that two CRs can both be effectively imaged. Compared with BP algorithm, the proposed 3D FPFA algorithm can achieve similar result, as shown in Fig. 6 (b), but with much reduced computing time. Besides, by using the SVA method, the high-level sidelobes can be effectively suppressed without reducing the resolution, as shown in Fig. 6 (c). With 64 randomly selected pairs of transceivers and 101 frequencies, the imaging result of the proposed T-IAA algorithm is shown in Fig. 6 (d), from which it can be observed that the sidelobes are much reduced. Furthermore, measured by TIC and TOC instructions in MATLAB and averaged by 50 trials, the running time of BP algorithm, 3D FPFA algorithm, 3D FPFA algorithm with SVA approach, and T-IAA algorithm are 7.76 s, 0.12 s, 0.48 s, and 1.50 s, respectively. This indicates that BP algorithm is most time-consuming and the proposed algorithms can reduce the computing time. Besides, since only 1/8 data is used by the proposed T-IAA algorithm, the memory usage is also reduced.

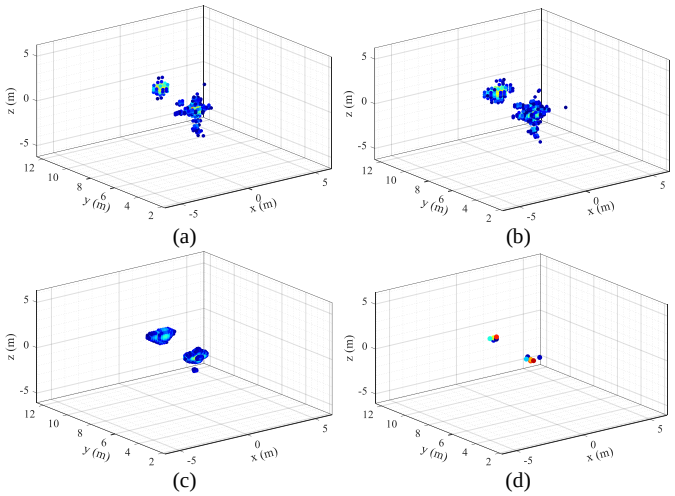

Fig. 6. Focused images obtained by (a) BP algorithm, (b) FPFA algorithm, (c) FPFA algorithm with SVA, and (d) T-IAA algorithm with 1/8 data.

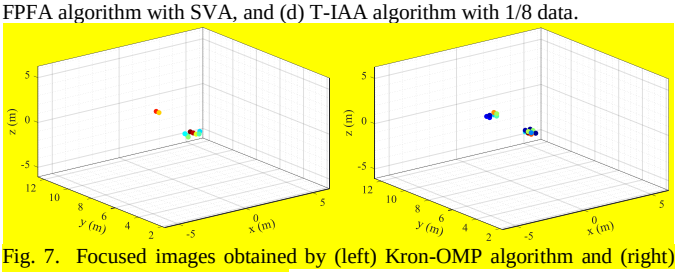

Fig. 7. Focused images obtained by (left) Kron-OMP algorithm and (right) NBOMP algorithm with 1/8 data.

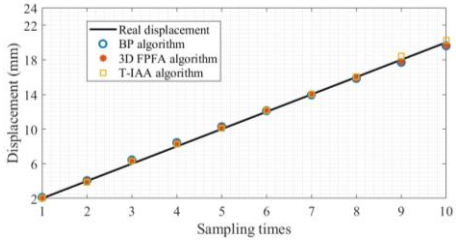

Fig. 8. Displacement estimation results obtained by different algorithms.

Apart from the proposed T-IAA algorithm, other T-CS algorithms can also be used to solve (14). For example, the imaging results obtained by Kron-OMP algorithm and NBOMP

algorithm [13] with 1/8 data are shown in Fig. 7. By comparing with Fig. 6 (d) and Fig. 7, it can be observed that the results of these three T-CS algorithms are similar, strong sidelobes can be effectively reduced. However, as mentioned in Section-III, OMP-type algorithms need to get the target number or the noise level to terminate the iterations, which is difficult to estimate. On the contrary, the T-IAA algorithm is nonparametric and can always converge within 10-15 iterations. Therefore, T-IAA algorithm maybe more suitable in practical applications.

Then, one of the CRs, which is mounted on a linear scanner, as indicated by the solid red circle in Fig. 5, is moved away from the radar system from 2 mm to 20 mm with a 2 mm step along the line of sight (LOS). The displacement estimation results obtained by BP algorithm, FPFA algorithm, and T-IAA algorithm are shown in Fig. 8. It can be learned that all these methods can achieve accurate displacement estimates. We note that, due to the influence of random selection, the joint T-IAA algorithm, which can be easily derived from the joint 2D IAA algorithm proposed in [16], is used in this case.

At last, a building with four floors is used as the target, as shown in Fig. 9. The purpose of this experiment is to validate the imaging performance of the designed system for distributed target 3D imaging. The imaging result obtained by BP algorithm and 3D FPFA algorithm with SVA approach are shown in Fig. 10 with a dynamic range of 25 dB. For BP algorithm, strong sidelobes make the imaging result difficult to understand. However, by using SVA approach, four layers and main parts of the building can be clearly observed by 3D FPFA algorithm. This result further demonstrates the effectiveness of the designed C-band cross-MIMO radar system and the proposed imaging algorithm.

Fig. 9. Experiment with a four-floor building as target.

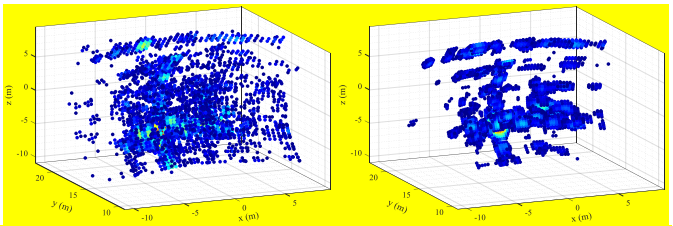

Fig. 10. Focused image of the building as distributed target obtained by (left) BP algorithm and (right) 3D FPFA algorithm with SVA approach.

CONCLUSIONS

A new methodology for real time 3D imaging and displacement measurement based on GBSAR interferometry has been presented. It is based on a 2D cross-MIMO radar system which allows an effective 2D aperture synthesis and a fast data acquisition. The SAR focusing algorithm is based on a pseudo-polar spherical coordinate. Experiments have been carried out to prove the concept of the proposed methodology using a C-band prototype. The advantages of the proposed methodology in terms of focusing accuracy has been studied using trihedral corner reflectors (CRs) deployed in the scene. The proposed cross-MIMO radar has also been tested in an interferometric configuration to measure the displacements of CRs, using the proposed focusing algorithms, and comparing the results with those provided by other traditional focusing algorithms. Future work will be devoted to the application of the cross MIMO prototype and focusing algorithms to the monitoring of structures, glaciers and landslides.

REFERENCES

[1] A. Di Pasquale, G. Nico, A. Pitullo, and G. Prezioso, "Monitoring strategies of earth dams by ground-based radar interferometry: How to extract useful information for seismic risk assessment," *Sensors*, vol. 18, pp. 244-271, 2017.

[2] G. Nico, G. Cifarelli, G. Miccoli, F. Soccodato, W. Feng, M. Sato, and M. Marini, "Measurement of Pier Deformation Patterns by Ground-Based SAR Interferometry: Application to a Bollard Pull Trial," IEEE Journal of Oceanic Engineering, PP(99), 2018. 10.1109/JOE.2018.2840399.

[3] D. Tarchi, F. Oliveri, and P. F. Sammartino, "MIMO radar and ground based SAR imaging systems: Equivalent approaches for remote sensing," *IEEE Trans. Geosci. Remote Sens.*, vol. 51, no. 1, pp. 425–435, Jan. 2013.

[4] W. Feng, L. Yi, and M. Sato, "Near range radar imaging based on block sparsity and cross-correlation fusion algorithm," *IEEE J. Sel. Topics Appl. Earth Observ. Remote Sens.*, DOI: 10.1109/JSTARS.2018.2797056.

[5] P. Guccione, M. Zonno, L. Mascolo, and G. Nico, "Focusing algorithms analysis for ground-based SAR images," in *Proc. IEEE Int. Geosci. Remote Sens. Symp.*, 2013, pp. 3895-3898.

[6] X. Zhuge and A. Yarovoy, "Frequency-wavenumber domain focusing under linear MIMO array configurations," in *Proc. IEEE Int. Geosci. Remote Sens. Symp.*, 2012, pp. 2125-2128.

[7] W. Feng, L. Yi, and M. Sato, "Near range radar imaging by SFCW linear sparse array," in *Proc. IEEE Int. Geosci. Remote Sens. Symp.*, 2017, pp. 5362-5365.

[8] J. Fortuny-Guasch, "A fast and accurate far-field pseudopolar format radar imaging algorithm", *IEEE Trans. Geosci. Remote Sens.*, vol. 47, no. 4, pp. 1187-1196, April 2009.

[9] K. Han, Y. Wang, X. Chang, W. Tan, and W. Hong, "Generalized pseudopolar format algorithm for radar imaging with highly suboptimal aperture length," *Sci. China Inf. Sci.*, vol. 58, no. 4, pp. 042304:1–042304:15, Apr. 2015.

[10] X. Zhuge and A. Yarovoy, "A sparse aperture MIMO-SAR-based UWB imaging system for concealed weapon detection," *IEEE Trans. Geosci. Remote Sens.*, vol. 49, no. 1, pp. 509-518, 2011.

[11] R. Zhu, J. Zhou, G. Jiang, and Q. Fu, "Range migration algorithm for near-field MIMO-SAR imaging," *IEEE Geoscience and Remote Sensing Letters*, vol. 14, no. 12, pp. 2280-2284, Dec. 2017.

[12] W. Qiu, J. Zhou, H. Zhao, Q. Fu, "Three-dimensional sparse turntable microwave imaging based on compressive sensing," *IEEE Geoscience and Remote Sensing Letters*, vol. 12, no. 4, pp. 826-830, 2015.

[13] C. F. Caiafa, and A. Cichocki, "Multidimensional compressed sensing and their applications," *Wiley Interdisciplinary Reviews: Data Mining and Knowledge Discovery*, vol. 3, no. 6, pp. 355-380, 2013.

[14] T. Yardibi, J. Li, P. Stoica, M. Xue, and A. B. Baggeroer, "Source localization and sensing: a nonparametric iterative adaptive approach based on weighted least squares," *IEEE Trans. Aerosp. Electron. Syst.*, vol. 46, pp. 425-443, Jan. 2010.

[15] M. J. Jahromi, and M. H. Kahaei, "Two-dimensional iterative adaptive approach for sparse matrix solution", *Electron. Lett.*, vol. 50, no. 1, pp. 45-47, 2014.

[16] W. Feng, Y. Guo, X. He, H. Liu, and J. Gong, "Jointly iterative adaptive approach based space time adaptive processing using MIMO Radar," *IEEE Access*, vol. 6, pp. 26605-26616, 2018.

[17] T. G. Kolda and B. W. Bader, "Tensor decomposition and applications," *SIAM Review*, vol. 51, no. 3, pp. 455–500, 2009.

[18] H. C. Stankwitz, R. J. Dallaire, and J. R. Fienup, "Nonlinear apodization for sidelobe control in SAR imagery," *IEEE Trans. Aerosp. Electron. Syst.*, vol. 31, no. 1, pp. 267-279, 1995.